

# Instabilities of buoyancy-driven coastal currents and their nonlinear evolution in the two-layer rotating shallow-water model. Part 1. Passive lower layer

J. GULA<sup>†</sup> AND V. ZEITLIN

Laboratoire de Météorologie Dynamique, ENS and University P. and M. Curie,  
24 rue Lhomond, 75231 Paris, France

(Received 1 October 2009; revised 16 April 2010; accepted 16 April 2010;  
first published online 30 June 2010)

Buoyancy-driven coastal currents, which are bounded by a coast and a surface density front, are ubiquitous and play essential role in the mesoscale variability of the ocean. Their highly unstable nature is well known from observations, laboratory and numerical experiments. In this paper, we revisit the linear stability problem for such currents in the simplest reduced-gravity model and study nonlinear evolution of the instability by direct numerical simulations. By using the collocation method, we benchmark the classical linear stability results on zero-potential-vorticity (PV) fronts, and generalize them to non-zero-PV fronts. In both cases, we find that the instabilities are due to the resonance of frontal and coastal waves trapped in the current, and identify the most unstable long-wave modes. We then study the nonlinear evolution of the unstable modes with the help of a new high-resolution well-balanced finite-volume numerical scheme for shallow-water equations. The simulations are initialized with the unstable modes obtained from the linear stability analysis. We found that the principal instability saturates in two stages. At the first stage, the Kelvin component of the unstable mode breaks, forming a Kelvin front and leading to the reorganization of the mean flow through dissipative and wave–mean flow interaction effects. At the second stage, a new, secondary unstable mode of the Rossby type develops on the background of the reorganized mean flow, and then breaks, forming coherent vortex structures. We investigate the sensitivity of this scenario to the along-current boundary and initial conditions. A study of the same problem in the framework of the fully baroclinic two-layer model will be presented in the companion paper.

**Key words:** gravity currents, shallow-water flows, waves in rotating fluids

---

## 1. Introduction

Coastal currents in the ocean are commonly produced by the joint effects of buoyancy and the Coriolis force. For example, the Atlantic water entering the Mediterranean Sea forms the Algerian current, remaining at the surface due to its low density. There exist many other examples of the same type such as the Leeuwin Current, the East Greenland Current, the Norwegian Coastal Current, etc. Such boundary currents generally become unstable, producing meanders and detachment

<sup>†</sup> Email address for correspondence: gula@lmd.ens.fr

of vortices away from the coast. Eventually these instabilities control the horizontal mixing by the current. They therefore play an important role in the distribution of the biogeochemical components and their transfer between basins.

A widely used idealized model for studying dynamics of coastal currents is the reduced-gravity rotating shallow-water model in the half-plane, where the effects of density stratification are modelled by a single reduced-gravity parameter, and the system is represented by a single-layer finite-depth constant-density fluid terminating at the free streamline (surface front). The lower layer is then assumed to be infinitely deep so that the pressure remains constant there. Linear stability of density-driven coastal currents with a surface front in such configuration in the inviscid limit has been investigated by Killworth & Stern (1982), Paldor (1983) and Kubokawa (1986). Killworth & Stern (1982) showed that a coastal density current is unstable to long-wave disturbances in two cases: when the mean potential vorticity (PV) increases towards the wall (coast) and the mean tangent velocity is zero at the wall, and when the mean flow is close to uniform PV, if the velocity of the current is reversed between the coast and the front. Paldor (1983) examined the linear stability of a current with zero PV, and Kubokawa (1986) demonstrated that for a zero-PV flow there is an instability produced by the resonance between a frontal trapped wave and a coastal trapped wave.

Although the reduced-gravity model is a good first approximation, it obviously neglects dissipative effects, including Ekman pumping, and oversimplifies stratification. The former may be, in principle, parameterized, for the sake of applications, and the latter may be taken into account by using a full two-layer rotating shallow-water model. In many situations, the lower layer cannot be considered dynamically inactive, and new and important phenomena appear in the dynamics when the lower layer has a finite vertical thickness. Killworth, Paldor & Stern (1984) examined a free front far away from the wall, overlying an active lower layer with no motion in the basic state, and showed that the front is always unstable to long-wave perturbations regardless the distribution of PV, with much larger growth rates than in the one-layer case. In such a two-layer model, the mean flow in the upper layer forces the density interface to tilt and hence PV in the lower layer decreases towards the surface front. The PV gradient then allows for the existence of vortical waves in the lower layer which can couple with a frontal wave and cause the instability. The stability of a coastal upwelling front in a two-layer shallow-water model was investigated by Barth (1989*a,b*) and a baroclinic-type instability was found. Paldor & Ghil (1991) studied a zero-PV front with an active lower layer and found vigorous short-wave instabilities whenever the slanting interface between the layers extends close to the bottom of the ocean. These short-wave instabilities are similar to the classical Kelvin–Helmholtz instability.

Experimental investigations of the instabilities of the coastal fronts were also carried out. Without giving an exhaustive review, let us mention the classical paper by Griffiths & Linden (1982), where adjustment and subsequent development of the instability of the fronts, with secondary vortex formation, was studied in the two-layer system in the rotating annulus for a wide range of depth ratios of the layers.

In the present (Part 1) and companion (Part 2) papers, we present a systematic study of the instability, including its nonlinear stage, of the density-driven coastal currents in the framework of one-layer (Part 1) and two-layer (Part 2) rotating shallow-water models in the inviscid limit. Despite its simplicity, the shallow-water model contains all essential ingredients of large-scale atmospheric and oceanic dynamics. Its physical transparency greatly helps while performing the linear stability analysis

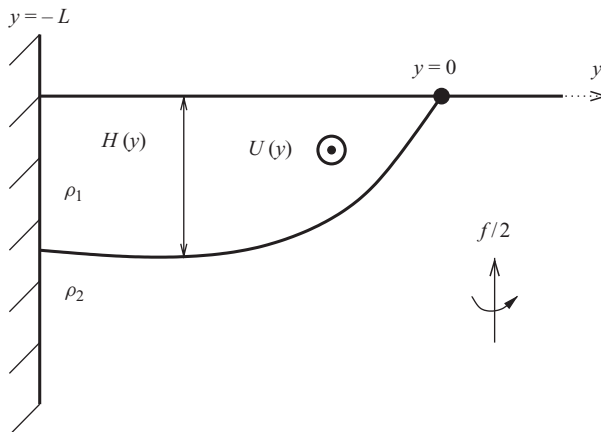


FIGURE 1. Schematic representation of the coastal current bounded by a density front.

and interpreting the results. At the same time, the model, both in one- and multi-layer versions, allows for efficient numerical treatment by using a new generation of high-resolution well-balanced finite-volume numerical schemes (Bouchut 2004, 2007; Bouchut & Zeitlin 2010). The shock-resolving property of these schemes is particularly important for the coastal configurations due to the dispersionless character of coastal Kelvin waves and their ability to break and form Kelvin fronts (Fedorov & Melville 1995). Also crucial in the context of the density fronts is the property of these numerical schemes to successfully treat drying (one-layer schemes) and outcropping (multi-layer schemes).

Below we will adopt a simple strategy consisting of identifying the most unstable modes of the coastal current configuration by a detailed stability analysis (we use the collocation method, Trefethen 2000), and then using them for initialization of the direct numerical simulations (DNS) with a finite-volume well-balanced scheme in order to study nonlinear evolution and saturation of the instability. A similar strategy with the same tools was recently used for studying a closely related but simpler problem of double density fronts (Scherer & Zeitlin 2008). In the present paper, we limit discussion to the one-layer model, and the analysis of two-layer configurations is dealt with in Part 2.

## 2. The model and the linear stability problem

### 2.1. Equations of motion, boundary conditions and steady states

A typical configuration of a density-driven coastal current is shown in figure 1. The undisturbed flow is bounded by a surface front at  $y=0$  and by a rigid vertical boundary at  $y=-L$ , and the density gradient between the fluid layers is sharp. As is well known, in the limit of infinitely large thickness of the lower layer the problem can be reformulated in terms of shallow-water equations with the reduced gravity replacing the standard gravity.

The equations of the rotating shallow-water model on the  $f$ -plane are

$$\left. \begin{aligned} u_t + uu_x + vv_y - fv &= -gh_x, \\ v_t + uv_x + vv_y + fu &= -gh_y, \\ h_t + (hu)_x + (hv)_y &= 0, \end{aligned} \right\} \quad (2.1)$$

where  $(x, y)$  and  $(u, v)$  are the zonal and meridional coordinates and velocity components, respectively,  $h$  is the fluid depth,  $g$  is the reduced gravity,  $f$  is the constant Coriolis parameter and the subscripts denote the corresponding partial derivatives.

The basic state is assumed to be steady. It is easy to see that geostrophically balanced fields  $u = U(y)$ ,  $v = 0$  and  $h = H(y)$ , where

$$U(y) = -\frac{g}{f}H_y(y), \quad (2.2)$$

provide an exact stationary solution of (2.1).

We linearize (2.1) about this steady state. The linearized equations, where  $u(x, y, t)$ ,  $v(x, y, t)$  and  $h(x, y, t)$  now denote the perturbations to the basic state fields, are

$$\left. \begin{aligned} u_t + Uu_x + vU_y - fv &= -gh_x, \\ v_t + Uv_x + fu &= -gh_y, \\ h_t + Uh_x &= -(Hu_x + (Hv)_y). \end{aligned} \right\} \quad (2.3)$$

We introduce the time scale  $f^{-1}$ , the horizontal scale  $L$ , which is the unperturbed width of the current, the velocity scale  $fL$  and the vertical scale  $(fL)^2/g$ . We will use only non-dimensional variables from now on without changing notation. Note that within this scaling the typical value of the velocity gives the value of the Rossby number. The following are the non-dimensional equations:

$$\left. \begin{aligned} u_t + Uu_x + vU_y - v &= -h_x, \\ v_t + Uv_x + u &= -h_y, \\ h_t + Uh_x &= -(Hu_x + (Hv)_y). \end{aligned} \right\} \quad (2.4)$$

We impose a boundary condition of no normal flow at the coast:  $v(-1) = 0$ . The boundary conditions at the front are

$$H(y) + h(x, y, t) = 0, \quad D_t Y_0 = v \quad \text{at } y = Y_0, \quad (2.5)$$

where  $y = 0$  is the location of the free streamline of the basic state,  $Y_0(x, t)$  is the position of the perturbed free streamline and  $D_t = \partial_t + u\partial_x + v\partial_y$  is the Lagrangian derivative. Physically, they correspond to the conditions that the fluid terminates at the boundary which is a material line. The linearized boundary conditions give

(1) the relation between the perturbation of the position of the free streamline and the value of the height perturbation:

$$Y_0 = -\frac{h}{H_y} \Big|_{y=0}, \quad (2.6)$$

(2) the continuity equation (2.4) evaluated at  $y = 0$ .

Hence, the only constraint to impose on the solutions of (2.4) is the regularity of solutions at  $y = 0$ .

The PV of the mean flow, in non-dimensional terms, is

$$Q(y) = \frac{1 - U_y}{H(y)}, \quad (2.7)$$

where the geostrophic equilibrium holds:

$$U(y) = -H_y(y). \quad (2.8)$$

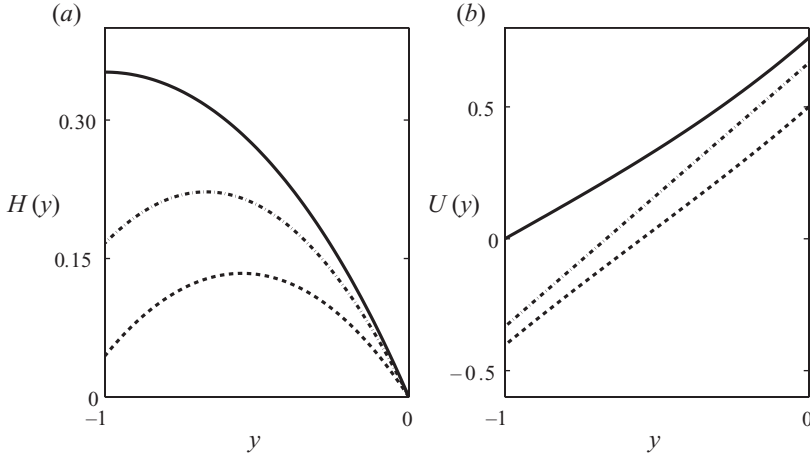


FIGURE 2. Examples of the basic state heights (a) and velocities (b) for constant-PV flows with  $Q_0=1$  and  $U_0=-\tanh(-1)$  (thick line),  $U_0=1/2$  (dotted line) and a zero-PV flow (dashed-dotted line).

The basic state height is then given by the solution of the following differential equation:

$$H_{yy}(y) - Q(y)H(y) + 1 = 0, \quad \text{with} \quad \begin{cases} H(0) = 0, \\ H_y(0) = -U_0, \end{cases} \quad (2.9)$$

where  $U(0)=U_0$  is the mean flow velocity at the front.

If we assume a zero-PV flow, i.e.  $Q(y)=0$ , this corresponds to the solution

$$\left. \begin{aligned} H(y) &= -U_0 y - \frac{y^2}{2}, \\ U(y) &= U_0 + y, \end{aligned} \right\} \quad (2.10)$$

which has been used by Stern (1980), Paldor (1983) and Kubokawa (1985). For the specific value  $U_0=1/2$ , this profile also coincides with that used by Griffiths, Killworth & Stern (1982), who investigated the instability of a current bounded by two surface fronts, yet the two problems are not equivalent due to the different boundary conditions at  $y=-1$ .

If we assume a constant-PV flow, i.e.  $Q(y)=Q_0 \neq 0$ , this corresponds to the solution

$$\left. \begin{aligned} H(y) &= \frac{1}{Q_0} [1 - U_0 \sqrt{Q_0} \sinh(\sqrt{Q_0} y) - \cosh(\sqrt{Q_0} y)], \\ U(y) &= U_0 \cosh(\sqrt{Q_0} y) + \frac{1}{\sqrt{Q_0}} \sinh(\sqrt{Q_0} y), \end{aligned} \right\} \quad (2.11)$$

which is similar to the solution used by Dahl (2005). The basic state height and velocity for both cases are plotted in figure 2.

## 2.2. Stability analysis by the collocation method

Assuming a harmonic form of the solution of (2.4) in the  $x$ -direction,

$$(u(x, y), v(x, y), h(x, y)) = (\tilde{u}(y), \tilde{v}(y), \tilde{h}(y)) \exp[i(kx - \omega t)], \quad (2.12)$$

we obtain an eigenvalue problem of order 3 which can be solved by applying the spectral collocation method as described in Trefethen (2000) and Poulin & Flierl

(2003). A complete basis of Chebyshev polynomials is used to obtain a discrete equivalent of the equations. This is achieved by evaluating (2.4) on a discrete set of  $N$  collocation points (typically  $N = 50\text{--}100$ ). The eigenvalues and eigenvectors of the resulting operator are computed with the Matlab routine ‘`eig`’. The occurrence of spurious eigenvalues is common in such discretization procedure. We therefore checked the persistence of the obtained eigenvalues by recomputing the spectrum with increasing  $N$ .

The disadvantage of the method is that it is not specially designed for treating singular eigenproblems. Indeed, the eigenproblem which results from injecting (2.12) into (2.4) has a well-known critical-layer singularity occurring whenever the real part of the eigen phase velocity of the perturbation  $c = \omega/k$  is equal to the local flow velocity:  $c = U(y)$ . Singularities give rise to the stable singular eigenmodes which form a continuous spectrum (see e.g. Vanneste 1998 for a similar albeit simpler geophysical fluid dynamics problem with critical layers). These modes have Dirac-delta or step function behaviour (depending on the variable), being in fact distributions, not functions. Discrete counterparts of such singular eigenmodes will be retrieved by the straightforward collocation method. They may be, nevertheless, easily identified by their singular profiles and the fact that they accumulate with increasing resolution (see below). A filtering procedure based on gradient limiters was applied to eliminate these pseudo-modes. The method was extensively tested in the related problem of coupled density fronts within the same model (Scherer & Zeitlin 2008), where more technical details may be found.

### 2.3. *Instabilities of density fronts as resonances between the eigenmodes*

The stability of the coastal current configurations with a front bounded by a wall has been investigated in previous studies. First, Killworth & Stern (1982) showed that a coastal density current in a one-layer model is unstable to long-wave disturbances in two cases: (i) when the mean PV gradient is positive at the wall and the mean velocity is zero at the wall, or (ii) when the current is not unidirectional (mean along-coast velocity and depth slope changing sign between the front and the coast; cf. figure 2) for flows with close to constant PV. Paldor (1983) examined the condition for stability for a basic flow with zero PV and showed that the current is stable provided the mean velocity of the basic flow exceeds  $fL$  (where  $f$  is the Coriolis parameter and  $L$  the width of the current), but he was not able to find any unstable waves when the flow did not satisfy this criterion.

It should be stressed that the most physically transparent way to understand instabilities of a given flow is to interpret them as the resonances between the eigenmodes and corresponding crossings of dispersion curves. The most known examples come from baroclinic interactions in a vertically sheared flow, e.g. Jones (1967) and Sakai (1989), but the same mechanism works for barotropic horizontally sheared flows, e.g. Satomura (1981) and Hayashi & Young (1987). It is, in particular, valid for the instabilities of the density fronts. Thus, the classical GKS instability, as described in Griffiths, Killworth & Stern (1982), for the one-layer reduced-gravity model of coupled density fronts (a gravity current that is bounded by two free streamlines), which has been already mentioned above, results from the resonance between two eigenmodes propagating along each front, respectively; cf. Pratt, Helfrich & Leen (2008), Scherer & Zeitlin (2008). We will refer to such modes trapped in the vicinity of the density front as frontal modes.

It should be mentioned that the instability of an isolated front in a one-layer reduced-gravity model, described in Killworth (1983) and Kubokawa (1985), is more

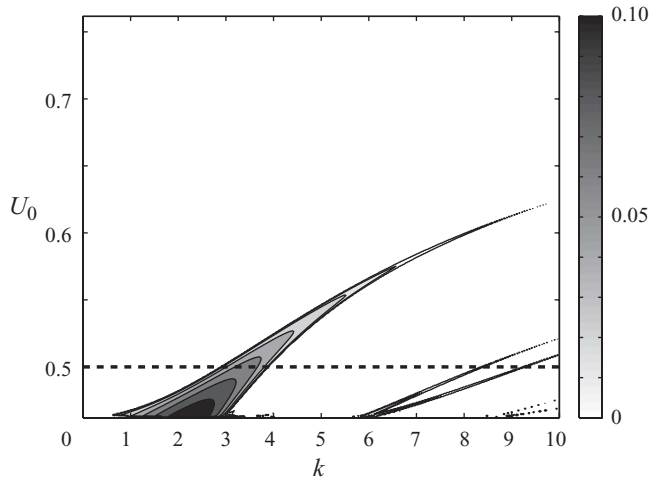


FIGURE 3. Stability diagram in the  $(U_0, k)$  plane for the constant-PV current. The values of the growth rates corresponding to grey levels are given in the right column.

complicated in nature than that of a pair of coupled fronts. It is a critical-layer-type instability which can be explained in terms of resonance between the frontal mode and a superposition of several singular modes from the continuous spectrum by the mechanisms described in Iga (1999), who showed that such instability can occur when the sign of the intrinsic phase speed of the non-singular mode (the frontal wave) and that of the gradient of the PV at the critical level are the same. A similar critical layer behaviour was noticed by Barth (1989*b*) in a configuration where the interface displacement has a rapid phase change across the point where the phase speed of the wave equals the mean flow velocity. An investigation of such configuration using the collocation method (not presented) perfectly matches this interpretation.

The coastal current configuration of this paper does contain the frontal waves trapped in the vicinity of the front, but also has another type of localized modes which are trapped near the coast, e.g. Kubokawa & Hanawa (1984). Kubokawa (1986) showed that the flow is indeed unstable when the condition of stability of Paldor (1983) is not satisfied, and identified the corresponding unstable modes for the zero-PV configuration as a resonance between a frontal wave and a coastal trapped wave. In the idealized case of vertical boundary we are considering that the coastal trapped waves are just Kelvin and Poincaré waves.

The frontal wave is described in Iga (1993) as a mixed Rossby-gravity wave, in a sense that it behaves like a Rossby mode as long as the wavenumber is small, but like a gravity mode when the wavenumber becomes large. Note that Hayashi & Young (1987), among others, refer to this mode as a Kelvin wave. More generally, the frontal mode can be interpreted as a vortical mode as in Meacham & Stephens (2001), in a sense of a wave that exists due to the PV gradient at the outcropping point, because this point may be interpreted as a point connecting the finite-depth layer with a layer of infinitesimal thickness (Boss, Paldor & Thompson 1996). We use denomination ‘frontal’ for such modes in what follows.

As an example of the just-described resonance interpretation of the instability of the coastal current, we present the results of linear stability analysis for the constant-PV flow corresponding to the basic state given by (2.11) (cf. figure 2). The growth rates of the most unstable modes are represented in figure 3 for  $U_0$  between the two limit values

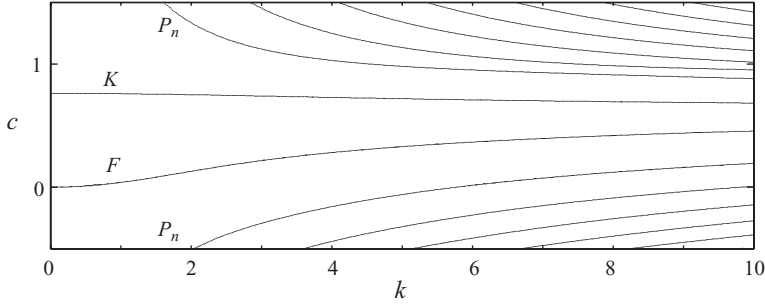


FIGURE 4. Dispersion diagram for  $U_0 = -\tanh(-1)$  and  $Q_0 = 1$ . The flow is unidirectional with zero tangent (zonal) velocity at the coast, and is stable.

corresponding to (a) zero velocity at the wall, resulting from  $U_0 = -\tanh(-1) \approx 0.75$ , and (b) zero height at the wall, resulting from  $U_0 = [1 - \cosh(-1)]/\sinh(-1) \approx 0.46$ .

Note that such basic state never satisfies Ripa's (1983) criterion within these limits. This criterion states that sufficient conditions for stability are the following:

$$\exists \alpha / \forall y \begin{cases} (U - \alpha) \frac{dQ}{dy} \leq 0, \\ (U - \alpha)^2 \leq H. \end{cases} \quad (2.13)$$

The first condition is always satisfied as  $Q = \text{const}$ . Due to the front at  $y = 0$  ( $H(0) = 0$ ), the only possible value to fulfil the second condition is  $\alpha = U_0$ . But the second condition can never be satisfied as  $(U_0 - U(-1))^2 \geq H(-1)$  is verified in the range of  $U_0$  plotted in figure 3.

Figure 4 represents the dispersion diagram in the phase speed–wavenumber plane for  $U_0 = 0.75$ , which corresponds to a stable case with zero velocity at the wall. We can use this case in order to identify various modes typical for the coastal current configuration. Two sets of Poincaré waves marked by  $P_n$  can propagate either at the coast or at the front, and are, as usual, almost dispersionless in the short-wave limit and strongly dispersive in the long-wave limit. The coastally trapped Poincaré waves, with amplitude decaying away from the coast, propagates in the positive direction while the frontally trapped Poincaré waves, with amplitude decaying away from the front, propagates in the negative direction. Kelvin mode (marked by  $K$ , with  $c_K \approx 0.75$  in the figure) propagates uniquely along the coast with low dispersion, and the frontal mode (marked by  $F$ , with  $c_F = 0$  at  $k = 0$ ) is quite dispersive for low wavenumbers:  $k < 10$ . Frontal mode, as well as other more familiar modes, can thus be clearly identified in dispersion diagrams. The resonances between different modes will lead to instabilities when  $U_0$  diminishes.

Figure 5 shows the dispersion diagram and corresponding growth rates as a function of  $k$  for  $U_0 = 0.5$  corresponding to the dashed line in figure 3. The flow has a counter current and is now likely to become unstable according to the criterion exposed earlier. There are indeed several instability zones. The main area of instability ( $k \approx 3.5$ ) corresponds to the resonance of the frontal mode and the Kelvin mode, as can be deduced from the intersection of the respective dispersion curves. Figure 6 shows the most unstable mode at  $k = 3.44$ , where one can recognize the characteristic structure of a Kelvin wave propagating along the coast ( $y = -1$ ) with no normal to the wall velocity, and the frontal mode at the front ( $y = 0$ ). Note the apparently balanced character (velocity following the isobars) of the frontal mode.

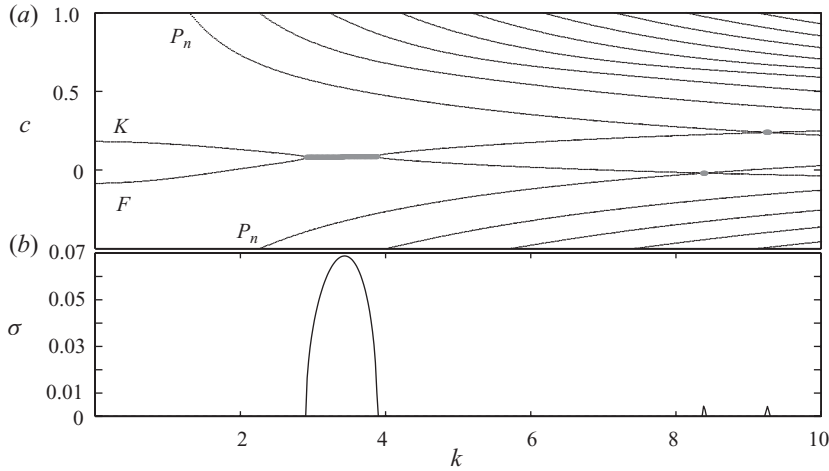


FIGURE 5. Dispersion diagram for  $U_0 = 0.5$  and  $Q_0 = 1$ . The flow is unstable. Crossings of the dispersion curves in (a) correspond to instability zones and non-zero growth rates in (b).

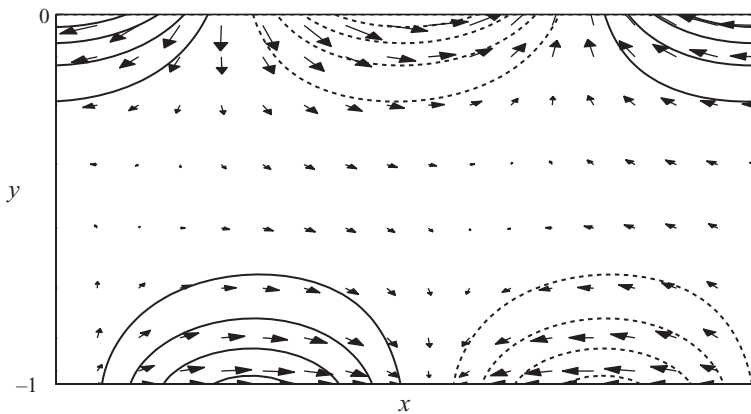


FIGURE 6. Height and velocity fields of the most unstable mode of figure 5 for  $k = 3.44$ , corresponding to the resonance between the Kelvin and the frontal mode. Only one wavelength is plotted. On this and similar figures below full lines correspond to positive and the dotted lines correspond to negative values.

Other instability zones, visible in figure 5 at wavenumbers higher than 8, and with much lower growth rates, correspond to the resonance of the Kelvin mode and the first frontally trapped unbalanced Poincaré mode, and the interaction of the first coastally trapped Poincaré mode with the balanced frontal mode, respectively. The structure of both unstable modes is presented in figure 7.

We also explored other basic state configurations with different heights and velocity profiles, with constant or non-constant PV, including zero PV, and obtained similar results, which we do not display. It should also be noted that a return flow is not a necessary condition for the instabilities to occur, as a basic state with zero mean velocity at the coast can be unstable if the mean PV gradient is positive at the coast.

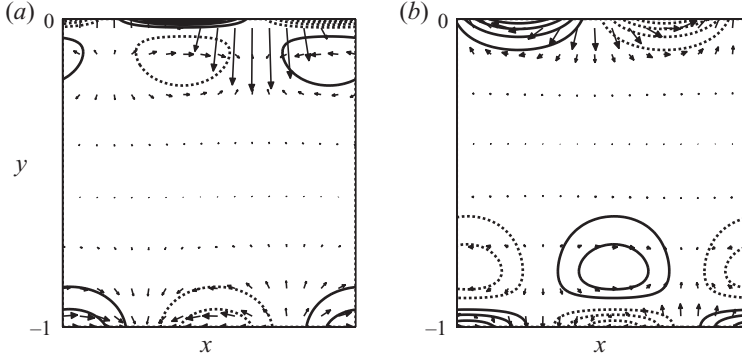


FIGURE 7. Height and velocity fields of higher wavenumber unstable modes of figure 5 for (a)  $k=8.4$  and (b)  $k=9.25$ . (a) Resonance between the Kelvin and a frontally trapped Poincaré mode and (b) resonance between a coastally trapped Poincaré mode and the frontal mode. Only one wavelength is plotted.

For example, a non-dimensional profile defined as

$$H(y) = -\left(U_0 y + \frac{1}{2}y^2 + \frac{1-U_0}{3}y^3\right), \quad (2.14)$$

$$U(y) = U_0 + y + (1-U_0)y^2 \quad (2.15)$$

satisfies the necessary conditions for the frontal instability.

We, thus, confirmed and extended earlier results on linear stability of the coastal currents in the one-layer reduced-gravity model, and got a transparent physical interpretation of the instability in terms of wave-wave resonance, which will allow for better understanding of its nonlinear stage. Below we will perform fully nonlinear DNS by initializing our numerical code with above-calculated unstable eigenmodes. It should be stressed that the collocation method gives the structure of the unstable modes with any desired accuracy.

### 3. Nonlinear evolution of the leading instability

#### 3.1. Brief reminder of the finite-volume methods for the rotating shallow-water model

Recent progress in finite-volume numerical schemes for shallow-water equations allows for implementationally simple and quantitatively reliable high-resolution modelling of fully nonlinear dynamics. We apply the high-resolution finite-volume numerical method by Bouchut (2004, 2007) which has the following properties, decisive in the context of outcropping coastal fronts/currents:

- (i) It preserves geostrophic equilibria (i.e. the stationary states in the case of a straight front).
- (ii) It resolves wave breaking and shock formation.
- (iii) It allows treatment of outcropping/drying.

It should be stressed that no explicit dissipation is introduced in the numerical scheme.

As was shown in previous applications of the method by Bouchut, Le Sommer & Zeitlin (2004, 2005) and Scherer & Zeitlin (2008), energy is extremely well preserved, the only significant energy loss being associated with sharp gradient formation (shocks or bores; Bouchut 2004) or with reconnection of the streamlines (barotropic Rossby

or frontal wave breaking; Bouchut *et al.* 2005 and Scherer & Zeitlin 2008), which produce localized dissipation zones. We briefly recall the main ingredients of the method. The shallow-water equations are discretized in the flux form on a regular grid within the framework of the finite-volume approach. The finite-volume scheme is then fully prescribed by the choice of the numerical flux function and the treatment of the remaining source terms associated with the Coriolis force. At each time step and in each direction, the Coriolis terms are reformulated following the apparent topography method first introduced by Bouchut (2004). The numerical flux function is associated with a relaxation solver adapted to treat topography, as proposed by Audusse *et al.* (2004). This choice of the numerical flux function ensures the ability of the numerical procedure to compute solutions of the shallow-water equations even in the case of terminating depth. The advantage of the scheme is that correct Rankine–Hugoniot (RH) conditions guaranteeing the decrease of energy across the shocks are automatically satisfied by the method, i.e. numerical viscosity is indeed a dissipation. The numerical simulations presented hereafter were obtained with typical resolution 0.005 and lasted for a couple of hours on a personal computer.

The numerical treatment of boundary conditions is usually done quite easily within the finite-volume framework (see Bouchut 2004). We typically work with periodic boundary conditions along the wall. The free-slip condition at the coast is realized by defining a symmetric ghost value in the cell beyond the wall, such as  $h_0^n = h_1^n$  and  $v_0^n = -v_1^n$  for adjacent cells separated by the wall. The sponge boundary conditions, if necessary, are realized by extending the computational domain beyond the physical one by several cells, and annihilating the return momentum fluxes.

### 3.2. Nonlinear evolution of the most unstable mode

We present below the results of the DNS of fully nonlinear evolution of the instability corresponding to the most unstable mode with  $k_0 = 3.44$  with the structure presented in figure 6. The boundary conditions are periodic in the zonal direction, with a period  $2n\pi/k_0$ . Thus, the periodicity with  $n$  wavelengths of the most unstable mode is imposed in the simulation. Since the numerical method allows for drying, we compute the solution on the  $[-1, 5]$  interval in the meridional direction with a free-slip condition at the wall at  $y = -1$  and a sponge boundary condition at  $y = 5$ . The front being initially situated at  $y = 0$ , we carefully check that the active fluid layer never reaches the boundary at  $y = 5$  during simulations.

The evolution of the height field in the  $(x, y)$ -plane is shown in figure 8 for  $n = 1$ .

As can be inferred from figure 9(a) where the time evolution of the energy of the perturbation is displayed, the instability initially develops exponentially (for  $t < 20$ ). The average growth rate during this first stage is  $\sigma \approx 0.06$ , which is relatively close to the value obtained from the linear stability analysis (see figure 5).

As we have shown earlier, the unstable mode under investigation is composed of a frontal and a Kelvin wave. It is known that Kelvin waves have a tendency to steepen, and to ultimately break (Bennett 1973), forming Kelvin fronts (Fedorov & Melville 1995). As usual (cf. Bouchut *et al.* 2005), the breaking process should enhance dissipation at the breaking location and, thus, contribute to the viscous saturation of the instability. Indeed, as shown in figure 10, where the zonal velocity of the flow close to the wall is plotted at different times during the initial development of the unstable mode, the steepening of the Kelvin wave does take place and its location does correspond to the enhanced dissipation zone displayed in figure 8, which thus finds its explanation. A closer view of the structure of the unstable mode after 30 inertial periods is presented in figure 11 and confirms the breaking-Kelvin-wave scenario.

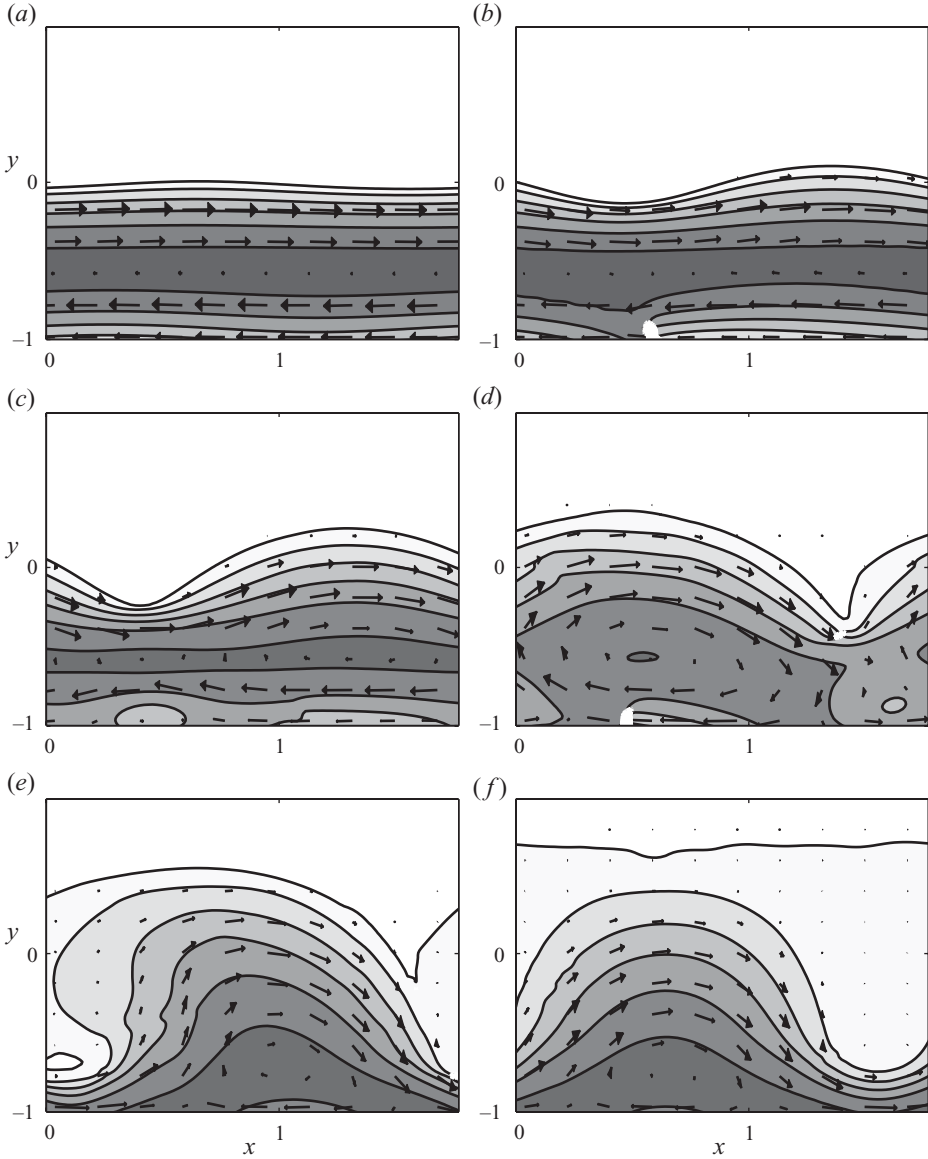


FIGURE 8. Levels of  $h(x, y, t)$  at the interval 0.05 at  $t=0, 30, 200, 340, 350, 500$  for the evolution of the most unstable mode of figure 6 corresponding to the basic flow with constant PV as defined by (2.11). Contours displayed are 0.01, 0.05, and further on at the interval 0.05. The arrows indicate the mass flux  $h v$ . The initial amplitude of the perturbation is 10% of the maximum depth of the basic state. The calculation domain is periodic in the  $x$ -direction and corresponds to one wavelength of the most unstable mode. Small white areas superimposed on the isolines of the height field close to the coast correspond to spatial distribution of the dissipation rate beyond the threshold 0.003 and up to a maximum value of 0.03. The dissipation rate is calculated as the deviation from the energy balance in each cell per time step in non-dimensional units.

A recently discovered feature of the Kelvin fronts is associated with secondary inertia-gravity-wave (IGW) emission (Fedorov & Melville 2000; LeSommer, Reznik & Zeitlin 2004). This emission is confirmed by our simulations, as is clear from the

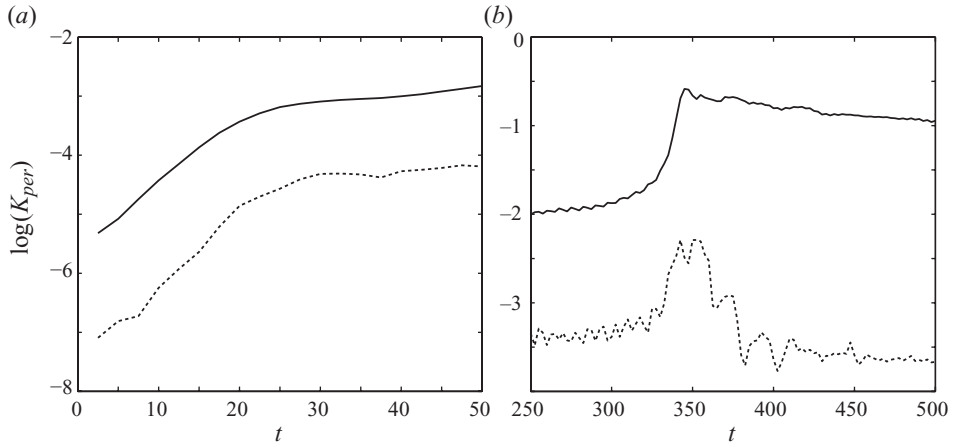


FIGURE 9. Logarithm of the kinetic energy  $K_{per}$  of the perturbation for the simulation of figure 8 (normalized by initial total kinetic energy) for mode  $k=1$  in  $x$  (thick line) and sum of the modes  $k > 1$  (dashed line), as a function of time.

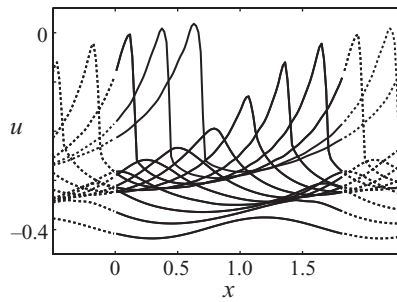


FIGURE 10. Evolution of the tangent (zonal) velocity of the flow at  $y = -L$  (at the wall) for  $t=0, 2.5, 5, 7.5, 10, 12.5, 15, 17.5, 20, 22.5, 25, 27.5$  (from lower to upper curves).

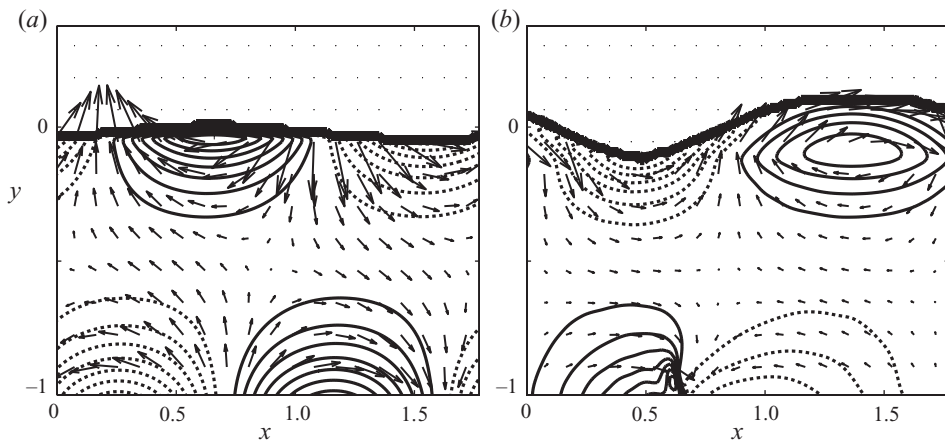


FIGURE 11. Height and velocity fields of the perturbation at  $t=0$  (a) and  $t=30$  (b). Kelvin front is clearly seen at the bottom of (b).

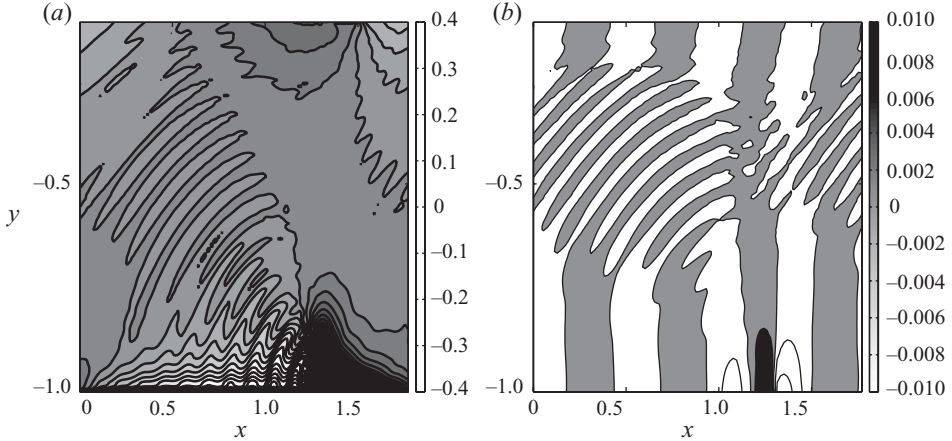


FIGURE 12. Horizontal divergence of the velocity field (a) and zonally filtered height field (b) at  $t = 20$  for the simulation of figure 8.

horizontal divergence and corresponding height perturbation fields presented in figure 12. Although in the aforementioned papers it was the IGW emission by equatorial Kelvin waves which was observed and explained, the argument is easily transposable to coastal Kelvin waves.

It should be noted that Kelvin wave breaking induces (a) significant interaction between the wave field and the mean flow, and (b) dissipation, yielding advective PV fluxes which irreversibly modify the PV distribution (cf. LeSommer *et al.* 2004; Bouchut *et al.* 2005). The amplitude of the mean zonal velocity is weakened at the wall, due to the steepening of the Kelvin mode and subsequent dissipation and wave–mean flow interactions thereafter. The mean flow is thus significantly modified and may give rise to new, secondary instabilities. This is what indeed happens.

As can be seen from figure 9(b), a second stage of the instability develops after some time, manifesting itself by a sharp rise of the energy of the perturbation. A  $k = k_0$  mode develops with a maximal growth rate  $\sigma \approx 0.05$ . The structure of this mode (the velocity and the depth of the flow with the zonal mean being removed) is represented in figure 13(a). We see a Rossby-like wave close to the wall which resonates with the (modified) frontal wave.

To understand this secondary instability, a linear stability analysis of the modified mean flow is needed. After the growth stage of the primary instability the mean zonal velocity of the flow is weakened close to the wall due to the breaking of the Kelvin mode, and the front is spread due to the growth of the frontal mode, as shown in figure 14.

We thus consider the mean flow of figure 14 (thick line) as a new basic state, and repeat the linear stability analysis. The corresponding dispersion diagram and growth rates are presented in figure 15, and the structure of the most unstable eigenmode is displayed in figure 16, where we see that a frontal mode is now resonating with a Rossby-like mode in a larger wavenumber range  $0 < k < 4$  than for the primary instability. This instability is of the Rossby–Rossby type, if we follow the classification of Sakai (1989).

A qualitative explanation of the modified stability properties of the flow may be given in terms of PV. The PV is no longer constant in the fluid layer, as a negative gradient of PV near the wall appears due to Kelvin wave breaking and related

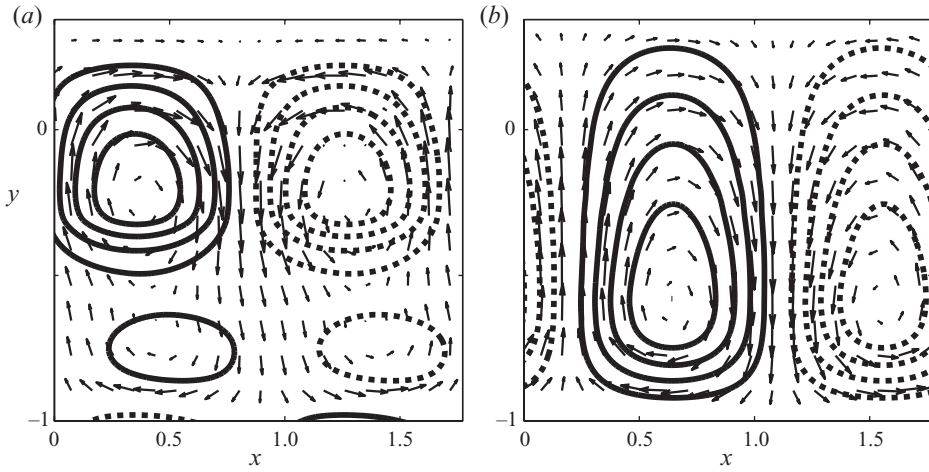


FIGURE 13. Height and velocity fields of the perturbation with  $k=k_0$  at  $t=335$  (a) and  $t=500$  (b).

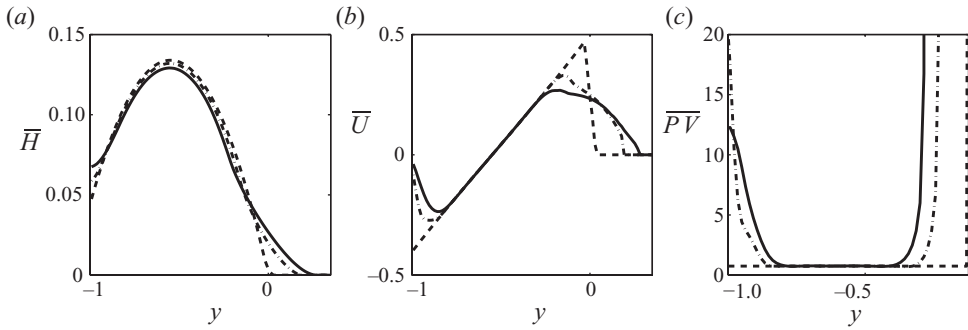


FIGURE 14. (a) Evolution of the mean zonal height, (b) mean zonal velocity and (c) mean zonal PV for the simulation of figure 8: dashed line, initial state ( $t=0$ ); dashed-dotted line: primary unstable mode saturated at  $t=40$ ; thick line: late stage ( $t=300$ ).

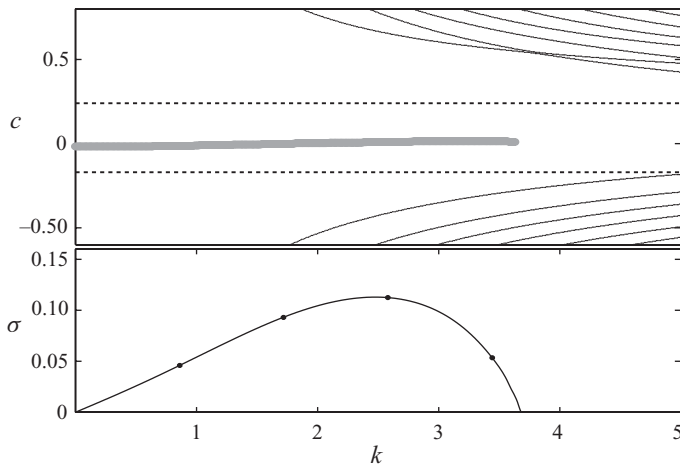


FIGURE 15. Dispersion diagram of the eigenmodes corresponding to the basic state profile of the flow at  $t=335$ , at the beginning of the secondary instability stage (see figure 14).

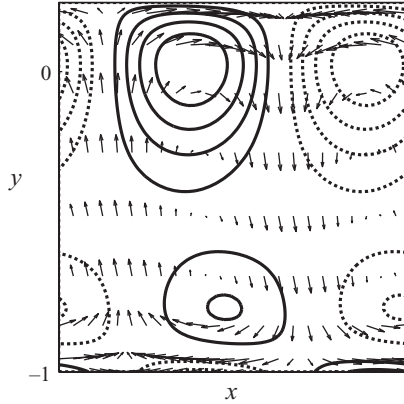


FIGURE 16. Height and velocity fields of the most unstable mode of figure 15 for  $k = k_0$ . Only one wavelength is plotted. Note the similarity with the mode observed in the simulation (figure 13).

dissipation as presented in figure 14. If we also take into account the positive PV gradient due to the drying at the front, the Rayleigh–Kuo criterion, namely that the horizontal PV gradient has to change sign for instability to occur, will then be satisfied by the flow. To support this reasoning, we present the evolution of the PV field in figure 17. It should be noted that simulations for the zero-PV basic state (not shown) exhibit a similar behaviour. The saturation of the primary instability leads to the formation of a negative gradient of PV near the wall and the development of the secondary instability as in the previous case, with a lower growth rate and a larger wavenumber, in accord with the linear stability results of §2.

As follows from figure 15, the growth rate of the secondary instability for the wavenumber  $k = k_0 = 3.44$  is  $\sigma = 0.056$ , which fits quite well the growth rate observed during the simulation (see figure 9). Note that it does not correspond to the largest possible growth rate of this instability which would be obtained for  $k = 2.5$ , because the periodic zonal condition of the numerical experiment does not allow for wavenumbers less than  $k_0 = 3.44$ . The instability then saturates via unstable Rossby-type breaking, as can be seen in figure 8 at  $t \approx 350$ . The flow reaches a new state of equilibrium after this stage, (see figure 8f), with anticyclonic vortex meanders. The corresponding filtered field (cf. figure 13) shows a Rossby wave slowly propagating with the mean flow.

The total energy loss during the whole simulation is about 20 % of the total initial energy, as shown in figure 18. It is non-negligible but stays quite acceptable compared to rather long duration ( $t = 500$ ) of the simulation. In the numerical scheme we are using, the numerical dissipation acts only in the zones of high gradients. The events of enhanced dissipation take place during the two stages of instability at the time of Kelvin and Rossby wave breaking, which is consistent with what was stated earlier. The slow monotonic decrease of energy during the whole simulation is explained by the fact that it is easy to generate micro shocks in the shallow regions of the fluid in the drying zone.

### 3.3. *The role of boundary conditions and manifestation of the instability in the initial-value problem*

As we have seen in the previous subsection, the choice of the along-current boundary condition does affect the nonlinear evolution of the instability at the second stage by

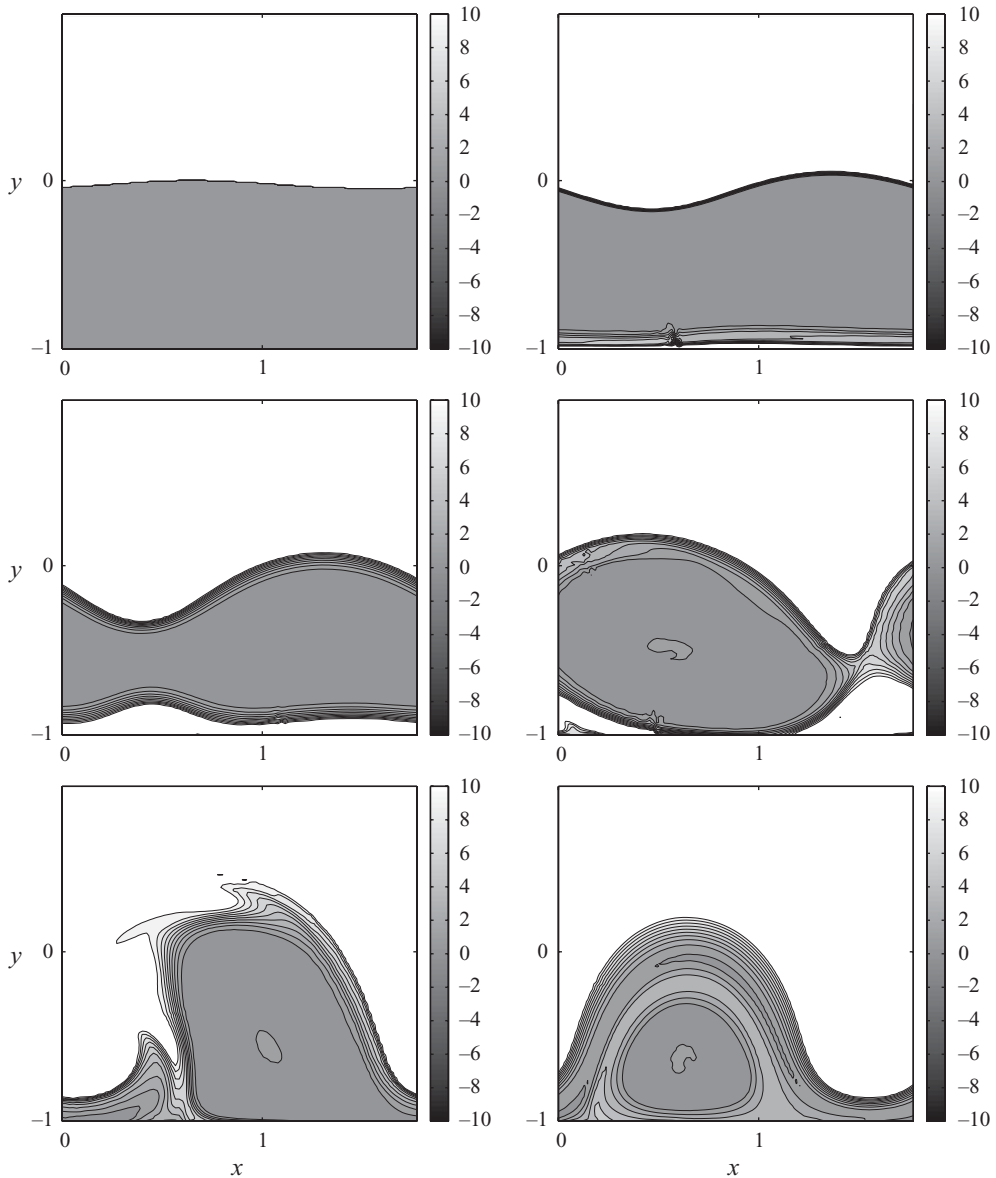


FIGURE 17. PV field corresponding to the simulation of figure 8 at  $t = 0, 30, 200, 335, 350, 500$ . Contours at interval 1.

selecting a specific unstable mode of the mean flow modified by the primary instability. In order to investigate the sensitivity of the nonlinear evolution scenario to this effect, we performed the same simulation with a quadrupled spatial period. This means that the development of perturbations with the wavelength up to four times longer than the wavelength of the most unstable mode was allowed. The corresponding evolution of the height field in the  $(x, y)$ -plane is shown in figure 19. The evolution of the kinetic energies of the perturbation modes with  $k = k_0, 0.75k_0$  and  $0.5k_0$  are plotted in figure 20.

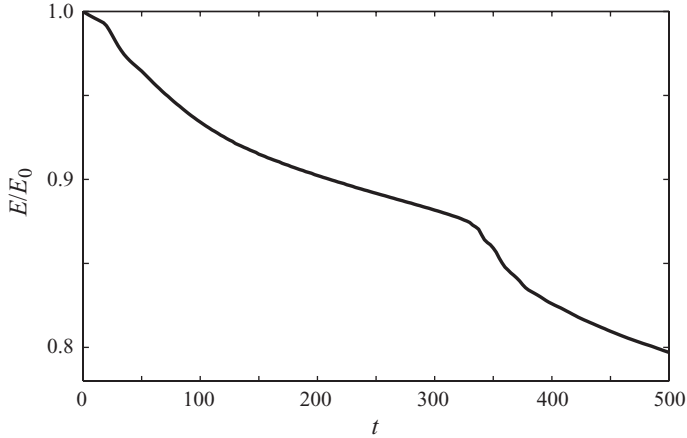


FIGURE 18. Time evolution of the total energy normalized by the initial energy for the evolution of the primary instability. The events of stronger decrease correspond to the events of Kelvin and Rossby wave breaking.

One can see that the primary instability develops in the same way as in the previous simulation for  $0 < t < 30$ . The  $k = k_0$  mode grows with a growth rate  $\sigma \approx 0.06$ , as expected from the linear stability analysis until the breaking event of the Kelvin mode. But then the evolution of the flow differs, as we now allow the development of modes with lower wavenumbers,  $k = 0.75k_0$ ,  $0.5k_0$  and  $0.25k_0$ . The evolution of the kinetic energy for each of these modes (figure 20) shows that they grow at the second stage of the instability with the growth rates  $\sigma \approx 0.05$ ,  $0.09$ ,  $0.07$  and  $0.04$  for  $k = k_0$ ,  $0.75k_0$ ,  $0.5k_0$  and  $0.25k_0$ , respectively. These are to be compared with the growth rates of the stability analysis of figure 15, which gives  $\sigma = 0.05$ ,  $0.1$ ,  $0.08$  and  $0.04$ , respectively. This means that, again, it is just the linearly unstable reorganized mean flow which is at the origin of secondary growing modes, and not e.g. the parametric instability of the primary unstable mode.

The filtered velocity and height fields of the secondary growing modes as given by the direct simulation are presented in figure 21. They are in very good agreement with the corresponding eigenmodes computed from the linear stability analysis which are plotted in figure 22 for the same wavenumbers, thus conforming the interpretation of the secondary growing modes as linearly unstable modes on the background of the mean flow modified by the development of the primary instability.

As to the nonlinear stage of the secondary instability, the presence of several growing modes with comparable growth rates leads to spatial modulation of the breaking Rossby-wave patterns, as can be seen in figure 19.

Similar simulations have been performed for other sizes of the zonal domain, giving results that support the same interpretation.

In the preceding subsections we deliberately initialized nonlinear simulations by superposing the most unstable spatially periodic mode onto the basic flow. Another question, however, arises: what is the role of the instability in the evolution of the localized initial perturbations of the basic flow?

In this (more realistic) context Stern (1980) studied finite-amplitude perturbations of a coastal current with zero PV and found several classes of perturbations which could steepen with time or block the transport in the current. Paldor (1988) used asymptotic expansion techniques to study perturbations and found the existence of

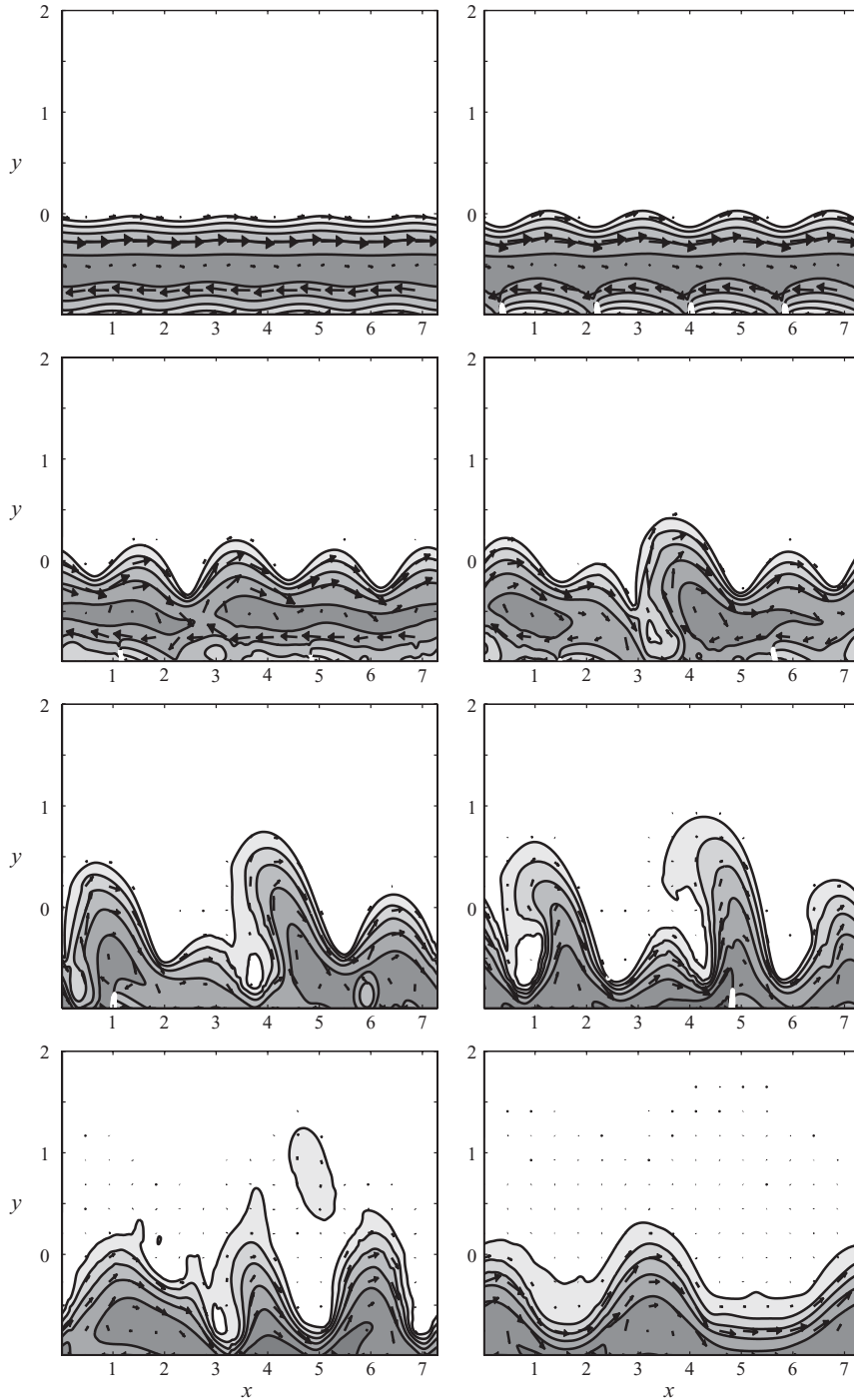


FIGURE 19. Levels of  $h(x, y, t)$  are shown at  $t = 0, 20, 130, 140, 150, 160, 200$  and  $500$  for the development of the most unstable mode of figure 6 corresponding to the basic flow with constant PV as defined by (2.11). Contours displayed are 0.01, 0.05, and further on at the interval 0.05. The arrows indicate the mass flux  $h\mathbf{v}$ . The initial amplitude of the perturbation is 10% of the maximum depth of the basic state. The calculation domain is periodic in the  $x$ -direction and corresponds to four wavelengths of the most unstable mode. Small white areas superimposed on the isolines of the height field close to the coast correspond to spatial distribution of the dissipation rate between 0.005 and 0.05 (the maximum value).

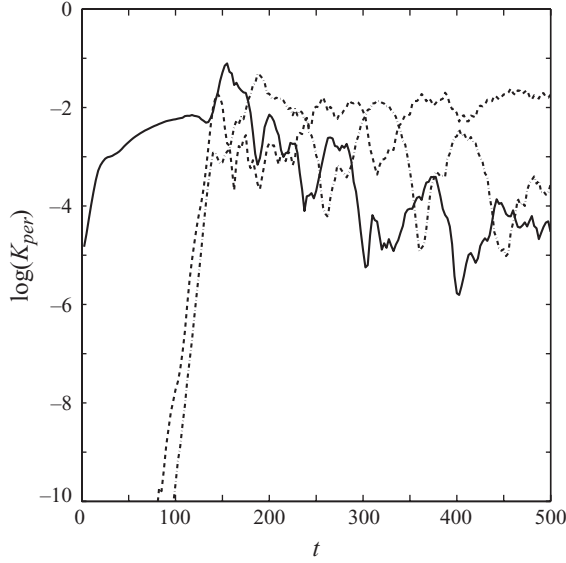


FIGURE 20. Logarithm of the kinetic energy  $K_{per}$  (normalized by the initial total kinetic energy) of the most energetic perturbation modes  $k=k_0$  in  $x$  (thick line),  $k=0.75k_0$  (dashed line) and  $k=0.5k_0$  (dashed-dotted line) as a function of time for the simulation of figure 19.

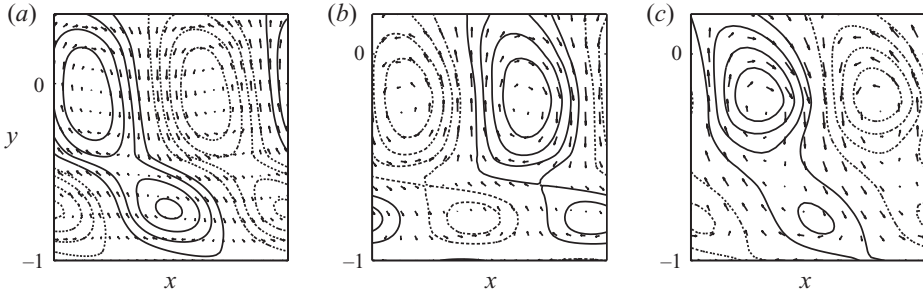


FIGURE 21. Height and velocity fields for the secondary unstable modes with wavenumbers (a)  $k=0.5k_0$ , (b)  $k=0.75k_0$  and (c)  $k=k_0$  for the simulation of figure 19 at  $t=140$ .

solitary and cnoidal waves, governed by the Korteweg–de Vries equation. Dahl (2005) investigated perturbations of arbitrary initial shape of a constant-PV current and found that the initial perturbation gives rise mainly to the two distinguished wave modes, the Kelvin wave and the frontal wave, while the rest of the perturbation is advected and slowly smeared out by the current.

To answer this question we have chosen a localized initial perturbation of the form

$$h(x, y) = Ae^{(-x/L_p)^2}, \quad (3.1)$$

with a smooth regularization in  $y$  at the front location  $y=0$ , and superposed it first on the stable basic flow with zero zonal velocity at the wall, and with dispersion diagram of figure 4. The corresponding evolution of the height field in the  $(x, y)$ -plane is shown in figure 23.

The  $x$ -coordinate has been rescaled (divided by time  $t=45$ ) in order to give the Doppler-shifted phase velocity of the different waves excited by the perturbation. One

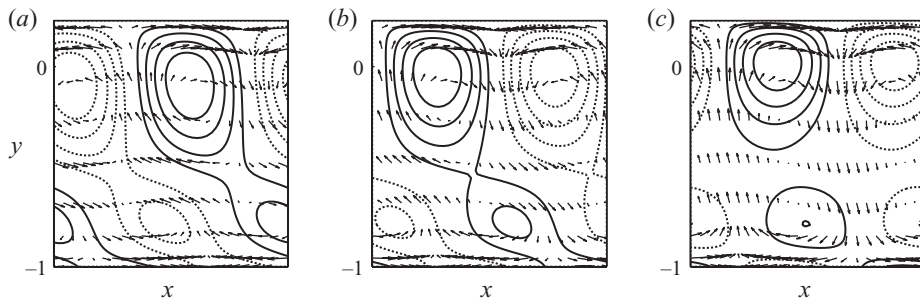


FIGURE 22. Height and velocity fields of the unstable modes with wavenumbers (a)  $k = 0.5k_0$ , (b)  $k = 0.75k_0$  and (c)  $k = k_0$  computed from the linear stability analysis of the reorganized mean flow (see figure 15).

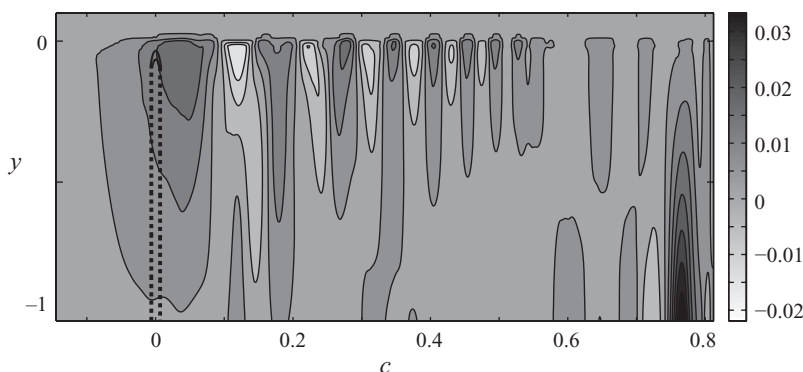


FIGURE 23. Levels of  $h(x, y, t)$  at  $t = 45$  for the evolution of a localized initial perturbation (dashed black line) imposed on a linearly stable basic state. The initial amplitude of the perturbation  $A$  is 0.05 and the width of the perturbation is  $L_p = 0.5$ .

can verify that the perturbation excites mainly the two types of waves described in the previous sections: the faster one with its maximum at the coast being a Kelvin wave and the slower one with its maximum at the front being a frontal wave. The comparison of the dispersion relation of these waves as deduced from figure 23, which provides both the phase speed and the corresponding wavelength, with that following from figure 4 shows that our interpretation is consistent. We thus recover weakly dispersive Kelvin waves with  $0.65 < c < 0.75$ , the maximum of their amplitude propagating in the direction of the current with the characteristic Kelvin wave speed  $c \approx \sqrt{gH(-1)}$ . The frontal waves have a greater dispersion  $0 < c < 0.5$ , the first mode being almost stationary, while higher modes propagate in the direction of the current. In this simulation with a stable basic flow the two families of waves just propagate at different velocities: one at the coast and one at the density front, without ‘feeling’ each other.

We then imposed the same initial perturbation on a linearly unstable flow with a return current at the coast. The frontal and the Kelvin waves are excited similarly by the perturbation but now, consistently with the resonance interpretation of the instability, their Doppler-shifted phase velocities are close. Figure 24 shows the perturbation height for such flow after  $t = 45$ . From this simulation we extract the phase speed of the frontal waves to be from  $c \approx -0.1$  for low  $k$  to  $c \approx 0.3$  for greater  $k$ , and the Kelvin waves phase speed from  $c \approx 0.2$  for low  $k$  to  $c \approx -0.1$  for

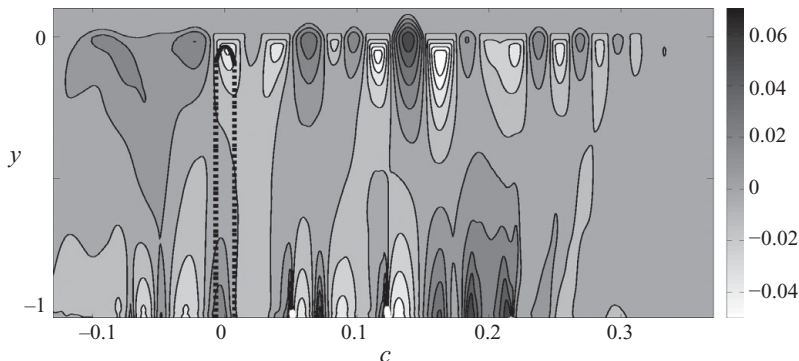


FIGURE 24. Same as in figure 23, but for a linearly unstable basic state, and with a rescaling in  $x$  in order to zoom into developing instability.

greater  $k$ . These results fit well the linear analysis of figure 5. As repeatedly stated before, the unstable character of the flow is due to the resonance between these two types of waves corresponding to a crossing between the two respective dispersion curves, i.e. close phase speeds in some range of wavenumbers. Such phase-locking is clearly visible in figure 24, the two types of waves having close wavenumbers and phase speeds in the domain  $0.1 < c < 0.18$ . Consistently, the amplitude of the perturbation height is growing in this area, roughly being twice higher than in the stable situation of figure 23 for  $0.1 \leq c \leq 0.3$ .

In both cases, we verified that the initial perturbation mainly excites the Kelvin and frontal waves. In the case of a linearly stable flow, the non-dispersive coastal wave propagates away in the direction of the current while the frontal modes manifest as stationary meanders due to the first frontal wave mode and moving meanders corresponding to the higher order modes. In the case of a linearly unstable flow, the subsequent evolution of the flow (not shown) shows that we recover the scenario described in the previous subsections, leading to the apparition of the secondary instability.

#### 4. Summary and concluding remarks

Linear instabilities of the coastal buoyancy-driven currents and their fully nonlinear evolution have been studied within the reduced-gravity rotating shallow-water model. By using the collocation method, we benchmarked the classical linear stability results on zero-PV fronts, and generalized them to non-zero-PV fronts. In both cases, we found instabilities due to the resonance of the frontal wave and the coastal Kelvin wave trapped in the current, and identified the most unstable long-wave mode.

We then studied the nonlinear evolution of the unstable modes with the help of a high-resolution well-balanced finite-volume numerical scheme for shallow-water equations. The simulations have been initialized both with the unstable modes obtained from the linear stability analysis and with localized perturbations. We found that the most unstable mode is growing to finite amplitude, and then saturates, leading to a reorganization of the mean flow, and hence of the PV field. The saturation of the primary instability is due to the breaking of its Kelvin-wave component, formation of Kelvin fronts with enhanced dissipation and emission of short-scale IGWs.

A linear stability analysis of thus modified mean flow shows that it is unstable to a secondary instability, of the type of the classical barotropic instability due to a change

of sign of the gradient of PV within the current. This scenario is verified in the DNS, showing that after the saturation of the first instability, the secondary instability leads to growth and ultimate breaking of the unstable Rossby-type mode, leading to the formation of coherent balanced vortex structures.

For a coastal current, the lower layer can rarely be considered dynamically inactive. The coupling between the two layers is likely to allow for different types of baroclinic interactions that were forbidden in the reduced-gravity model to appear. The barotropic instability discussed in the previous sections, and subsequent finite-amplitude development of the flow will also be modified by the presence of an active lower layer. For example, upper layer anticyclones which form in the final state of the reduced-gravity simulations could couple with lower layer cyclones and propagate away from the coast. We address these questions in Part 2 of the present study, which is the subject of the companion paper (Gula, Zeitlin & Bouchut 2010).

In this relation, sensitivity of the results to the physics at the interface between the layers should be discussed. The question of the choice of correct RH conditions to impose at internal hydraulic jumps in two-layer flows was intensely discussed in the literature (e.g. Klemp, Rotunno & Skamarock 1997 and references therein), without a definite answer. Yet, as we have seen above, the saturation of primary instabilities is strongly conditioned by the Kelvin wave breaking, and the details of this process may depend on the RH conditions, which are not unique in the two-layer system. Various choices have been proposed, e.g. energy conservation and momentum decrease across the jump (Klemp *et al.* 1997). In our numerical implementation of the one-layer model the standard RH conditions related to momentum and mass conservation, and energy decrease hold. (Energy plays the role of the gas dynamics entropy in this context; it is to be stressed that our numerical scheme automatically verifies the entropy inequalities, which is one of its big advantages.) What is important in the present context is that our numerical scheme, due to its well-balanced property, respects the PV conservation and gives correct PV generation behind the shocks (Bouchut *et al.* 2005).

However, as the one-layer model was used above for modelling a limiting case of the two-layer one, the question arises: to what RH conditions in this latter it corresponds? We will address this question in more detail in the companion paper (Gula *et al.* 2010), and should only mention here that the numerical scheme of Bouchut & Zeitlin (2010), which we use for full two-layer modelling, is consistent with the RH momentum conditions for the individual layers, and in the limit of the lower layer depth going to infinity gives results identical to those presented above, for the same initial conditions. This proves self-consistency of our approach, but does not exclude other possibilities, eventually corresponding to different sets of RH conditions. However, no consistent numerical implementations for the two-layer system with such ‘non-standard’ RH conditions exist, as to our knowledge.

This work was supported by ANR project FLOWING (BLAN06-3 137005) and Alliance project 15102ZJ.

#### REFERENCES

- AUDUSSE, E., BOUCHUT, F., BRISTEAU, M.-O., KLEIN, R. & PERTHAME, B. 2004 A fast and stable well-balanced scheme with hydrostatic reconstruction for shallow water flows. *SIAM J. Sci. Comput.* **25**, 2050–2065.
- BARTH, J. A. 1989a Stability of a coastal upwelling front, 1. Model development and a stability theorem. *J. Geophys. Res.* **94**, 10844–10856.

- BARTH, J. A. 1989*b* Stability of a coastal upwelling front, 2. Model results and comparison with observations. *J. Geophys. Res.* **94**, 10857–10883.
- BENNETT, J. R. 1973 A theory of large-amplitude Kelvin waves. *J. Phys. Oceanogr.* **3**, 57–60.
- BOSS, E., PALDOR, N. & THOMPSON, L. 1996 Stability of a potential vorticity front: from quasi-geostrophy to shallow water. *J. Fluid Mech.* **315**, 65–84.
- BOUCHUT, F. 2004 *Nonlinear Stability of Finite Volume Methods for Hyperbolic Conservation Laws, and Well-Balanced Schemes for Sources*. Frontiers in Mathematics Series, Birkhäuser.
- BOUCHUT, F. 2007 Efficient numerical finite-volume schemes for shallow-water models. In *Nonlinear Dynamics of Rotating Shallow Water: Methods and Advances* (ed. V. Zeitlin), vol. 2, pp. 189–256. Edited Series on Advances in Nonlinear Science and Complexity, Elsevier.
- BOUCHUT, F., LE SOMMER, J. & ZEITLIN, V. 2004 One-dimensional rotating shallow water: nonlinear semi-geostrophic adjustment, slow manifold and nonlinear wave phenomena. Part 2. High-resolution numerical simulations. *J. Fluid Mech.* **514**, 35–63.
- BOUCHUT, F., LE SOMMER, J. & ZEITLIN, V. 2005 Breaking of equatorial waves. *Chaos* **15**, 013503-1–013503-19.
- BOUCHUT, F. & ZEITLIN, V. 2010 A robust well-balanced scheme for multi-layer shallow water equations. *Discrete Contin. Dyn. Syst. Ser. B* **13**, 739–758.
- DAHL, O. H. 2005 Development of perturbations on a buoyant coastal current. *J. Fluid Mech.* **527**, 337–351.
- FEDOROV, A. V. & MELVILLE, W. K. 1995 Propagation and breaking of nonlinear Kelvin waves. *J. Phys. Oceanogr.* **25**, 2519–2531.
- FEDOROV, A. V. & MELVILLE, W. K. 2000 Kelvin fronts on the equatorial thermocline. *J. Phys. Oceanogr.* **30**, 1692–1705.
- GRIFFITHS, R. W., KILLWORTH, P. D. & STERN, M. E. 1982 Ageostrophic instability of ocean currents. *J. Fluid Mech.* **117**, 343–377.
- GRIFFITHS, R. W. & LINDEN, P. F. 1982 Laboratory experiments in fronts. Part I: Density-driven boundary currents. *Geophys. Astrophys. Fluid Dyn.* **19**, 159–187.
- GULA, J., ZEITLIN, V. & BOUCHUT, F. 2010 Instabilities of buoyancy driven coastal currents and their nonlinear evolution in the two-layer rotating shallow water model. Part 2. Active lower layer. *J. Fluid Mech.* (submitted).
- HAYASHI, Y.-Y. & YOUNG, W. R. 1987 Stable and unstable shear modes of rotating parallel flows in shallow water. *J. Fluid Mech.* **184**, 477–504.
- IGA, K. 1993 Reconsideration of Orlandi's instability theory of frontal waves. *J. Fluid Mech.* **255**, 213–236.
- IGA, K. 1999 Critical layer instability as a resonance between a non-singular mode and continuous modes. *Fluid Dyn. Res.* **25**, 63–86.
- JONES, W. L. 1967 Propagation of internal gravity waves in fluids with shear flow and rotation. *J. Fluid Mech.* **30**, 439–448.
- KILLWORTH, P. D. 1983 Long-wave instability of an isolated front. *Geophys. Astrophys. Fluid Dyn.* **25**, 235–258.
- KILLWORTH, P. D., PALDOR, N. & STERN, M. E. 1984 Wave propagation and growth on a surface front in a two-layer geostrophic current. *J. Mar. Res.* **42**, 761–785.
- KILLWORTH, P. D. & STERN, M. E. 1982 Instabilities on density-driven boundary currents and fronts. *Geophys. Astrophys. Fluid Dyn.* **22**, 1–28.
- KLEMP, J. B., ROTUNNO, R. & SKAMAROCK, W. C. 1997 On the propagation of internal bores. *J. Fluid Mech.* **331**, 81–106.
- KUBOKAWA, A. 1985 Instability of a geostrophic front and its energetics. *Geophys. Astrophys. Fluid Dyn.* **33**, 223–257.
- KUBOKAWA, A. 1986 Instability caused by the coalescence of two modes of a one-layer coastal current with a surface front. *J. Oceanogr. Soc. Japan* **42**, 373–380.
- KUBOKAWA, A. & HANAWA, K. 1984 A theory of semigeostrophic gravity waves and its application to the intrusion of a density current along a coast. Part 1. *J. Oceanogr. Soc. Japan* **40**, 247–259.
- LESOMMER, J., REZNIK, G. & ZEITLIN, V. 2004 Nonlinear geostrophic adjustment of long-wave disturbances in the shallow-water model on the equatorial beta-plane. *J. Fluid Mech.* **515**, 135–170.
- MEACHAM, S. P. & STEPHENS, J. C. 2001 Instabilities of gravity currents along a slope. *J. Phys. Oceanogr.* **31**, 30–53.

- PALDOR, N. 1983 Stability and stable modes of coastal fronts. *Geophys. Astrophys. Fluid Dyn.* **27**, 217–228.
- PALDOR, N. 1988 Amplitude–wavelength relations of nonlinear frontal waves on coastal currents. *J. Phys. Oceanogr.* **18**, 753–760.
- PALDOR, N. & GHIL, M. 1991 Shortwave instabilities of coastal currents. *Geophys. Astrophys. Fluid Dyn.* **58**, 225–241.
- POULIN, F. J. & FLIERL, G. R. 2003 The nonlinear evolution of barotropically unstable jets. *J. Phys. Oceanogr.* **33**, 2173–2192.
- PRATT, L. J., HELFRICH, K. & LEEN, D. 2008 On the stability of ocean overflows. *J. Fluid Mech.* **602**, 241–266.
- RIPA, P. 1983 General stability conditions for zonal flows in a one-layer model on the  $\beta$ -plane or the sphere. *J. Fluid Mech.* **126**, 463–489.
- SAKAI, S. 1989 Rossby–Kelvin instability: a new type of ageostrophic instability caused by a resonance between Rossby waves and gravity waves. *J. Fluid Mech.* **202**, 149–176.
- SATOMURA, T. 1981 An investigation of shear instability in a shallow water. *J. Met. Soc. Japan* **59**, 148–167.
- SCHERER, E. & ZEITLIN, V. 2008 Instability of coupled geostrophic density fronts and its nonlinear evolution. *J. Fluid Mech.* **613**, 309–327.
- STERN, M. E. 1980 Geostrophic fronts, bores, breaking and blocking waves. *J. Fluid Mech.* **99**, 687–703.
- TREFETHEN, L. N. 2000 *Spectral Methods in Matlab*. SIAM.
- VANNESTE, J. 1998 A nonlinear critical layer generated by the interaction of free Rossby waves. *J. Fluid Mech.* **371**, 319–344.